THE JOURNAL OF PHYSICAL CHEMISTRY C
A JOURNAL OF THE AMERICAN CHEMICAL SOCIETY

pubs.acs.org/JPCC Article

Defect-Dependent Surface Phase Transformation on 1*T*-TiS_2 Assisted by Water

Xue Chen, Meng Song, Liujiang Zhang, Ranran Zhang, Lei Zhang, Wei Tong, Yuyan Han, Xingyu Gao, Yimin Xiong,* Hai Xu,* and Liang Cao*

Cite This: *J. Phys. Chem. C* 2023, 127, 3462−3469 Read Online

ABSTRACT: The phase transformation from the TiS_2 to TiS on the surface of bulk 1*T*-TiS_2 crystals is achieved by thermal vacuum annealing. This is demonstrated by a combination of photoemission spectroscopy, electron paramagnetic resonance spectroscopy, and Raman spectroscopy. The chemical interaction between TiS_2 and surface-adsorbed H_2O molecules is expected to assist this transformation. Especially, the transformation temperature is found to depend on the natural defects present in the TiS_2 crystals. Ti interstitial (Ti_i) and S vacancy (S_v) defects hinder TiS_2 to TiS transformation, whereas Ti-OH species facilitate the phase transformation. These results not only provide a valuable insight into the water-assisted phase transformation modulated by defects but also highlight a potential strategy for designing an unusual TiS_2-TiS heterostructure through a combination of phase and defect engineering.

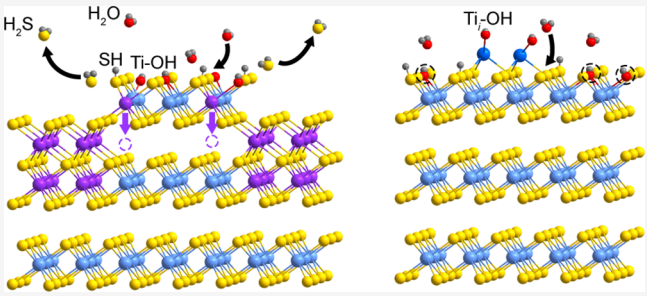

■ INTRODUCTION

Transition metal dichalcogenide (TMDC)-based heterostructures have broad application prospects in the field of optoelectronics,[1] catalysis,[2] and energy storage and conversion.[3] Moreover, novel physical phenomena, such as nonlinear optics,[4] spin−orbit physics,[5] and valleytronics,[6] are explored due to the breaking of symmetry at the interface of heterostructures.[7] The structural phase modulation is one of the efficient strategies for the fabrication of heterostructures to control the physical properties and to realize new functionalities.[8−10] Strainless and ohmic contacted heterostructures have been built by the partial phase transformation, which show enhanced performance by avoiding the lattice mismatch and contact problem.[11−14] For example, the thermal-driven transformation from semiconducting 2*H*-$MoTe_2$ to one-dimensional (1D) metallic Mo_6Te_6 leads to a 1D/2D metal−semiconductor heterostructure with reduced contact resistance,[15] which improves the supercapacitor performance.[16] In addition, it is found that defects, which exist naturally in TMDCs, play an important role in the phase transformation of TMDCs. Te vacancies in the 2*H*-$MoTe_2$ crystals trigger the phase transformation from 2*H*-$MoTe_2$ to metallic monoclinic 1*T*′-$MoTe_2$, which naturally fabricates an ohmic heterophase homojunction with increased carrier mobility.[17] As a consequence, understanding the phase transformation and effects of defects is of great significance for phase and defect engineering of heterostructure devices.

Titanium sulfide (TiS_2) exhibits great potential in energy storage and conversion, owing to its high performance, low cost, and earth abundance.[18,19] Various defects, including Ti interstitials (Ti_i), S vacancies (S_v), and oxidized Ti-O species, as illustrated in Figure 1, and Ti Frenkel pair and Ti vacancies (Ti_v) are reported to alter its physical and chemical properties.[20] Despite the advanced intrinsic and defect-tunable properties, the structural instability of the TiS_2 materials degrades its application capabilities, such as poor long-term cycle performance of TiS_2-based metal-ion batteries. So far, the introduction of Ti_v or S_v defects has significantly improved the cycle performance of the TiS_2 electrode for potassium-ion batteries,[21,22] implying that certain defects could improve the structural stability.[23] The rich natural defects and corresponding tunable structural instability make TiS_2 an ideal platform to investigate the effect of defects on structural evolution, which is critical for promising heterostructure construction and its practical device applications.

In this article, the surface phase transformation of TiS_2 depending on its intrinsic defects was identified by the results of photoemission spectroscopy (PES), electron paramagnetic resonance (EPR) spectroscopy, and Raman spectroscopy. The mechanism of this transformation was proposed by the joint effects of thermal annealing and chemical TiS_2-H_2O inter-

Received: November 21, 2022
Revised: January 25, 2023
Published: February 8, 2023

https://doi.org/10.1021/acs.jpcc.2c08140
J. Phys. Chem. C 2023, 127, 3462−3469

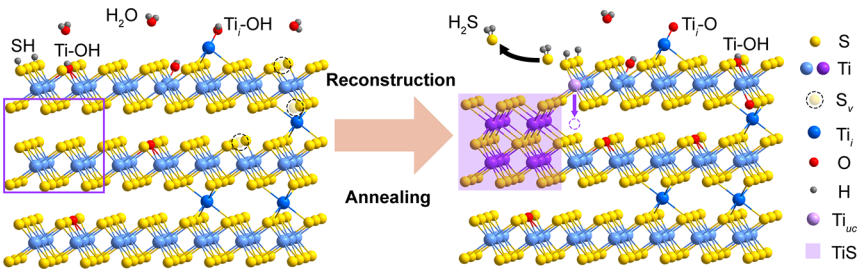

Figure 1. Schematic illustration of the surface TiS_2 to TiS transformation assisted by TiS_2-H_2O interaction. The left panel represents (i) the natural defects of S_v, Ti_i, and Ti-O species in the as-grown 1*T*-TiS_2 crystals and (ii) surface-adsorbed H_2O molecules, surface S-H, Ti-OH, and Ti_i-OH groups resulting from the TiS_2-H_2O or Ti_i-H_2O interaction. The right panel represents the thermal-driven formation of H_2S molecules and under-coordinated Ti-atoms (Ti_{uc}) and subsequent TiS transformation resulting from Ti_{uc} displacement to the octahedral sites in the van der Waals (vdW) gap.

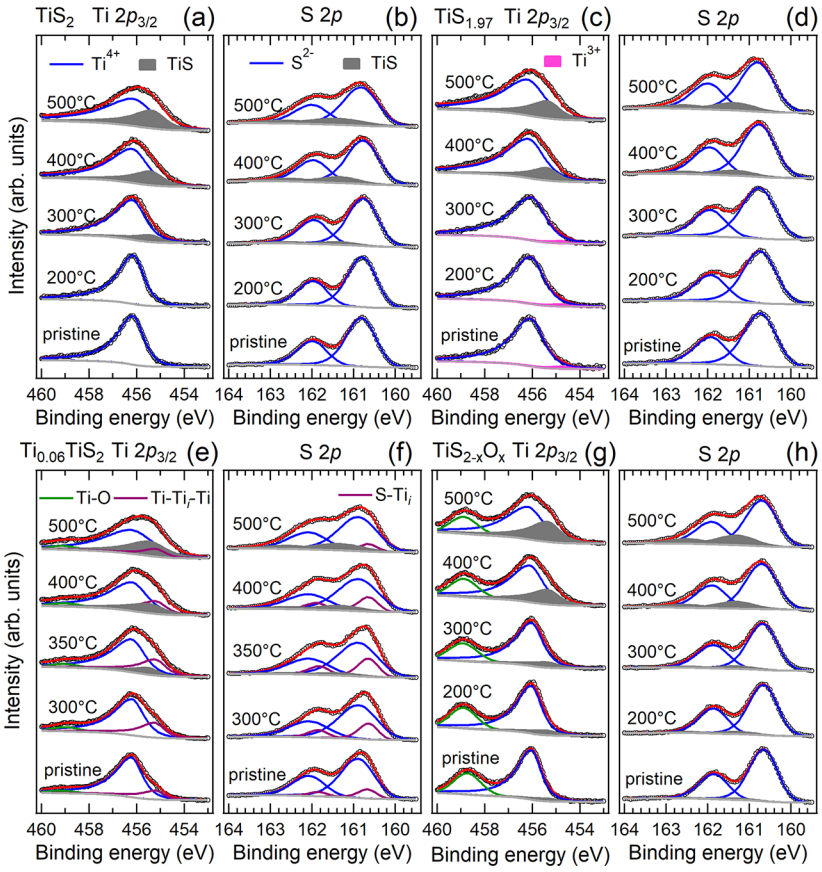

Figure 2. Evolution of Ti $2p_{3/2}$ and S 2p core-level spectra and corresponding fitting curves for (a, b) 1*T*-TiS_2, (c, d) $TiS_{1.97}$, (e, f) $Ti_{0.06}TiS_2$, and (g, h) $TiS_{2-x}O_x$ upon thermal annealing. The purple and green lines represent the Ti_i and Ti-O signals, respectively. The lines filled with pink and gray are related to the S_v and TiS species, respectively. The intensities are normalized to the corresponding Ti^{4+} and S^{2-} intensity of pristine samples.

action. The chemical reaction between the surface sulfur atoms and the adsorbed water plays a dominant role with the formation of H_2S species, leading to a surface phase transformation. This phase transformation then results in a new surface phase of TiS and fabricates a TiS/TiS_2 heterostructure spontaneously. Our findings can be extended to other TMDCs and shed light on the large-scale preparation of heterostructures and even Janus materials.

■ EXPERIMENTAL METHODS

TiS_2 single crystals with various defects were synthesized by a chemical vapor transport technique according to the method reported before.[24] First, titanium (99.99%, Alfa Aesar) and sulfur powder (99.8%, Alfa Aesar) with different molar ratios of Ti:S = *x*:2 (*x* = 0.95, 1, and 1.1) were sealed in the quartz tubes with the transport agent iodine (I_2) under vacuum and then heated up in a two-zone furnace for 144 h with different hot zone temperatures (650 °C) and cold zone temperatures (550 °C). Three batches of crystals named TiS_2 (Ti:S = 0.95:2), $Ti_{0.06}TiS_2$ (Ti:S = 1.1:2), and $TiS_{2-x}O_x$ (Ti:S = 1:2) were collected at the end of tubes placed in the cold zone after cooling down to room temperature. $TiS_{1.97}$ crystals were synthesized with a molar ratio of Ti:S = 0.95:2 at higher temperatures (hot zone temperature of 900 °C and cold zone

https://doi.org/10.1021/acs.jpcc.2c08140
J. Phys. Chem. C 2023, 127, 3462−3469

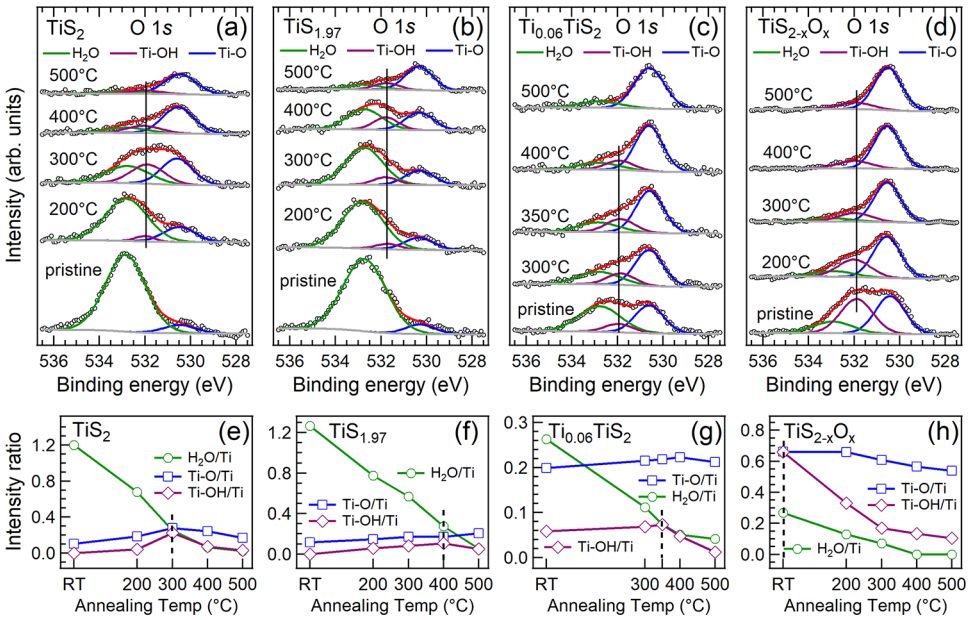

Figure 3. O 1s core-level spectra and corresponding fitting curves for (a) 1*T*-TiS_2, (b) $TiS_{1.97}$, (c) $Ti_{0.06}TiS_2$, and (d) $TiS_{2-x}O_x$ upon thermal annealing. The green lines, blue lines, and purple lines represent the surface-adsorbed H_2O molecules, Ti-O component, and Ti-OH groups, respectively. Relative intensities of the H_2O, Ti-O and Ti-OH species normalized to Ti $2p_{3/2}$ and their evolution as a function of the annealing temperature for (e) 1*T*-TiS_2, (f) $TiS_{1.97}$, (g) $Ti_{0.06}TiS_2$, and (h) $TiS_{2-x}O_x$ samples.

temperature of 800 °C). All the collected samples were stored in an Ar-protected glovebox before further characterization.

The structure of the as-synthesized samples was characterized at room temperature by X-ray diffraction (XRD) with Cu K_α radiation by a diffractometer (Rigaku-TTR3). Four studied crystals were cleaved in the atmosphere and transferred to the ultrahigh vacuum chamber with a base pressure of 2×10^{-9} mbar for PES characterization. The PES setup is equipped with a monochromatic Al K_α (1486.6 eV) X-ray source together with a SPECS PHOIBOS 100 hemispherical electron energy analyzer. Thermal vacuum annealing was performed in the same PES chamber at selected temperatures for 30 min. And the core-level spectroscopy of Ti 2p and S 2p was performed *in situ* after cooling down to room temperature. Finally, the annealed four crystals were collected and stored in an Ar-protected glovebox.

The four annealed crystals were cut to pieces for EPR and Raman characterization. EPR characterization was performed by a Bruker EMXplus 10/12 device (equipped with an Oxford ESR910 liquid helium cryostat) at 2 K. The Raman spectra were performed at room temperature by using a French Horiba J.Y. T64000 Raman spectrometer with a 532 nm laser. The sport size of the laser is around 5 μm. The annealed crystals were then cleaved for further Raman characterization.

■ RESULTS AND DISCUSSION

The stoichiometric 1*T*-TiS_2 and other three defective crystals of $TiS_{1.97}$, $Ti_{0.06}TiS_2$, and $TiS_{2-x}O_x$ containing S_v, Ti_i, and oxidized Ti-O species, respectively, were synthesized and the high crystallinity of the synthesized samples was identified by XRD, as shown in Figure S1 (see the Supporting Information). The positions of diffraction peaks remain almost constant for the stoichiometric TiS_2 and other three defective crystals, implying that the defects have less influence on the long-range order. To identify the defects and examine the evolution of chemical composition and binding environment upon thermal vacuum annealing conditions, the PES measurements were performed. Figure 2a,b shows a series of Ti $2p_{3/2}$ and S 2p core-level spectra for a stoichiometric 1*T*-TiS_2 crystal. The corresponding fitting curves are also displayed with the parameters summarized in Table S1 (see the Supporting Information). The single Ti $2p_{3/2}$ peak at ~456.2 eV and single S 2p doublet with S $2p_{3/2}$ peak at ~160.8 eV are ascribed to regular Ti^{4+} and S^{2-} ions, respectively, which both agree well with our previous PES results.[25] Upon annealing, the binding energies (BEs) of Ti^{4+} and S^{2-} associated peaks and their intensity ratio (Ti^{4+}/S^{2-}) remain almost constant. The spectral profile remains unchanged upon 200 °C annealing. After 300 °C annealing, the new features (filled with gray color) corresponding to a lower BE Ti $2p_{3/2}$ component (~455.4 eV) and a higher BE S $2p_{3/2}$ component (~161.2 eV) appear, indicating a charge redistribution between Ti- and S-atoms. The relative intensities of new components gradually increase upon further increasing annealing temperature. These new features are attributed to the TiS species. (i) The Ti:S ratio is close to 1:1. (ii) The possibility of the Ti_2S_3 species with a Ti:S ratio close to 1 can be ruled out because the BEs of Ti $2p_{3/2}$ and S 2p features for Ti_2S_3 are both lower than those for TiS_2.[26] (iii) The reported TiS_3 species are also excluded because the BE difference of 1.4 eV between two features associated with S_2^{2-} pairs and the isolated S^{2-} atoms[27] is larger than 0.4 eV extracted from the S 2p spectra in this study.

For $TiS_{1.97}$ crystals with S_v defects, the S_v-associated Ti^{3+} components give rise to a new feature with an ~1.3 eV lower BE in the Ti $2p_{3/2}$ spectra [cf. Figure 2c], but no new features in the S 2p spectra [cf. Figure 2d].[28] A Ti:S ratio of 1:1.97, as shown in the formula, is determined from the intensity of Ti $2p_{3/2}$ and S $2p_{3/2}$ normalized with respect to average matrix relative sensitivity factors.[29] A nominal S_v content of 0.03 is confirmed by the intensity ratio of Ti^{3+}/Ti^{4+} (cf. Table S2, Supporting Information).

https://doi.org/10.1021/acs.jpcc.2c08140
J. Phys. Chem. C 2023, 127, 3462−3469

For the $Ti_{0.06}TiS_2$ crystals containing Ti_i defects, the Ti $2p_{3/2}$ and S 2p spectra display lower BE Ti_i shoulders located at ~455.2 eV [cf. Figure 2e] and ~160.6 eV [cf. Figure 2f], respectively.[19,25] A nominal Ti_i content of 0.06 is yielded from the intensity ratio of Ti_i/Ti^{4+} (cf. Table S3, Supporting Information).[25] In addition, Ti-O/Ti-OH species resulting from a slight oxidation give rise to a higher BE peak at ~459.0 eV in the Ti $2p_{3/2}$ spectra.[30,31] This high BE component becomes apparent in the Ti $2p_{3/2}$ spectra for the $TiS_{2-x}O_x$ crystals containing abundance of Ti-O/Ti-OH species, as shown in Figure 2g. $Ti_{0.06}TiS_2$ and $TiS_{2-x}O_x$ crystals contain both Ti_i and oxidized Ti-O/Ti-OH species. Ti_i defects are found to be dominant in $Ti_{0.06}TiS_2$ crystals, whereas oxidized Ti-O/Ti-OH species dominate in $TiS_{2-x}O_x$ crystals, as revealed by the Ti $2p_{3/2}$ core-level spectra.

Upon annealing, the TiS species are also investigated in the above-mentioned three defective samples at different annealing temperatures, and the relative intensities show an increasing trend upon higher annealing temperatures. The temperatures at which the TiS species are detectable are 400 °C for $TiS_{1.97}$ [cf. Figure 2c,d] and 350 °C for $Ti_{0.06}TiS_2$ [cf. Figure 2e,f], which are higher than 300 °C for TiS_2. In contrast, the TiS species are detectable in the as-cleaved $TiS_{2-x}O_x$ sample before annealing treatment, as shown in Figure 2g,h.

It is thus found that the presence of both S_v and Ti_i defects hinders TiS_2 to TiS transformation, as revealed by higher phase transformation temperatures. However, the abundance of Ti-O(H) species facilitates the transformation by reducing the corresponding temperature even down to room temperature.

The O 1s core-level spectra can provide important information on the TiS_2 to TiS transformation. Figure 3a−d shows the O 1s core-level spectra and corresponding fitting curves for four studied samples. The peak parameters are listed in Table S5. Figure 3a displays the O 1s core-level spectra for a 1*T*-TiS_2 crystal. The dominant peak centered at ~532.8 eV and a shoulder at ~530.4 eV extracted from fitting curves are attributed to physisorbed H_2O molecules on the TiS_2 surface and the Ti-O species, respectively, which agree well with literature reports.[32−36]

Upon annealing, the BEs of both H_2O and Ti-O features keep constant, whereas their intensities vary obviously. H_2O feature is negligible after annealing at 500 °C, which is lower than the synthesis temperature of crystals. This implies that the physisorbed H_2O molecules on the crystal surface are most likely due to atmosphere exposure. An additional feature lying between H_2O and Ti-O components develops at ~531.8 eV after 200 °C annealing and preserves upon further annealing. This feature is attributed to newly formed Ti-OH species associated with the chemical interaction between TiS_2 and H_2O.[37] The Ti-OH species have been also found at the H_2O/TiO_2 interface and give rise to a component lying between features associated with physisorbed H_2O and TiO_2.[32,38]

All three H_2O, Ti-O, and Ti-OH components are also detected for three defective samples with almost constant BE, as shown in Figure 3b−d. The Ti-OH peak is detected even at room temperature for $Ti_{0.06}TiS_2$ and $TiS_{2-x}O_x$ crystals, implying that the dissociation of surface-adsorbed H_2O molecules into H and OH species and subsequent formation of Ti-OH species occur at room temperature for $Ti_{0.06}TiS_2$ and $TiS_{2-x}O_x$ crystals. This indicates that Ti_i and Ti-O species can provide sufficient electron to O-atoms to release H,[39,40] which is essential to water splitting. In contrast, TiS_2 and $TiS_{1.97}$ are not good candidates for water splitting at room temperature.

Figure 3e shows the relative intensities of H_2O, Ti-O, and Ti-OH components referred to the intensity of Ti $2p_{3/2}$ and their evolution as a function of the annealing temperature, which provide a valuable insight on the TiS_2 to TiS transformation. The intensity of the H_2O peak decreases rapidly due to desorption of H_2O molecules and dissociation of H_2O into H and OH species resulting from the TiS_2-H_2O chemical interaction. The H-atom is expected to bond to surface S-atoms forming S-H groups and the OH species are bonded with surface Ti-atoms and/or Ti_i forming Ti-OH and/or Ti_i-OH groups (cf. Figure 1). In addition, the H_2 molecules are formed resulting from the breaking of TiO-H and/or S-H bonds, leading to the formation of Ti-O species.[41,42] The newly formed Ti-OH and Ti-O species explain the increase of Ti-OH and Ti-O components until 300 °C annealing. After then, the intensities of both Ti-OH and Ti-O components decrease, implying the further dissociation of Ti-O bonds and TiO-H species into O and H, which facilitates H_2O evolution and desorption.

For $TiS_{1.97}$ crystals, the H_2O intensity decreases almost linearly upon annealing [cf. Figure 3f]. The intensities for Ti-O components increase slightly upon annealing. The temperature at which the intensity for the Ti-OH/Ti_i-OH species decreases (denoted as $T_{\text{Ti-OH}}$) is found to be 400 °C. The evolution of all three components for $Ti_{0.06}TiS_2$, as shown in Figure 3g, follows almost the same trends as that for TiS_2 with $T_{\text{Ti-OH}}$ occurring at 350 °C, and after 500 °C annealing, the $Ti_{(i)}$-OH component disappears completely. The intensities of all three components for $TiS_{2-x}O_x$ decrease upon annealing [cf. Figure 3h]. The occurrence of $T_{\text{Ti-OH}}$ at room temperature indicates that H_2O molecules have reacted with $TiS_{2-x}O_x$ even before annealing.

It is worth noting that $T_{\text{Ti-OH}}$ [guided by dashed lines in Figure 3e−h] are in line with the TiS_2 to TiS transformation temperatures extracted from Ti $2p_{3/2}$ and S 2p core-level spectra.

To rule out the generation of chalcogenide vacancies during thermal annealing, which may contribute to phase transformation,[43] EPR measurements were conducted at 2 K and are shown in Figure 4. The presence of Ti^{3+} resulting from electron trapping in S_v for $TiS_{1.97}$ yields a characteristic EPR spectrum with $g = 2.03$,[44,45] which is consistent with the PES results. After 500 °C annealing, the Ti^{3+}-associated signal disappears. No EPR signals are detectable for left three as-

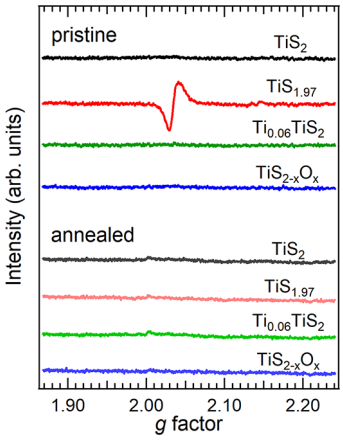

Figure 4. EPR spectra obtained at 2 K for four as-grown crystals and four crystals after 500 °C thermal vacuum annealing.

https://doi.org/10.1021/acs.jpcc.2c08140
J. Phys. Chem. C 2023, 127, 3462−3469

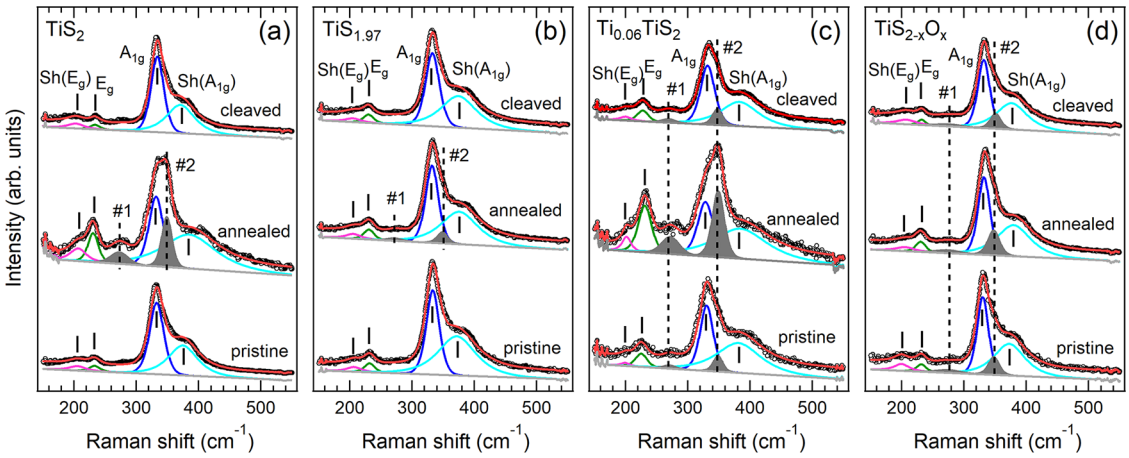

Figure 5. Raman spectra obtained using a 532 nm laser collected at room temperature for (a) 1*T*-TiS_2, (b) $TiS_{1.97}$, (c) $Ti_{0.06}TiS_2$, and (d) $TiS_{2-x}O_x$ and the corresponding fitting curves. All the Raman spectra are normalized to maximum intensity for clarity.

grown crystals and crystals after thermal annealing, ruling out the presence of either S_v or Ti_v. This indicates that the generation of S_v and Ti_v is not likely for TiS_2 crystals upon vacuum annealing, which is against to previous reports.[21,22]

To confirm the TiS_2 to TiS transformation and its spatial distribution (surface *vs* bulk), the Raman spectra were performed and are shown in Figure 5. As shown in the Raman spectra for 1*T*-TiS_2, the out-of-plane A_{1g} mode and corresponding shoulder Sh(A_{1g}) and in-plane E_g mode and corresponding shoulder Sh(E_g) are extracted to be of ∼332, ∼380, ∼230, and ∼205 cm^{-1}, respectively, which are consistent with the literature.[25] After 500 °C annealing, two additional peaks (labeled by #1 and #2) corresponding to the vibrational modes of TiS at ∼275 and ∼348 cm^{-1} become evident,[25] confirming the TiS_2 to TiS transformation. The surface of annealed samples is then cleaved with Scotch tape. The #1 and #2 peaks vanish, while the vibrational peaks for TiS_2 restore. Similar behaviors, including the emergence/enhancement of TiS-associated #1 and #2 peaks after annealing and disappearance/suppression after cleaving, are observed for $TiS_{1.97}$, $Ti_{0.06}TiS_2$, and $TiS_{2-x}O_x$ samples, suggesting that the TiS_2 to TiS transformation is surface limited. The intensities of #1 and #2 peaks are found to be much more intense for annealed TiS_2 and $Ti_{0.06}TiS_2$ crystals. This is due to the inhomogeneous surface spatial distribution of the newly formed TiS phase. This is supported by the Raman spectra acquired from different spatial positions on the 500 °C annealed TiS_2 crystal (cf. Figure S2). This inhomogeneity may be explained by the insufficient H_2O exposure. A sufficient amount of H_2O exposure in vacuum may lead to complete surface TiS_2 to TiS transformation initially, which deserves a further investigation.

As illustrated in Figure 1, the stripping of terminal S-atoms associated with the formation of H_2S molecules and the subsequent displacement of Ti_{uc} to underlying octahedral sites in the vdW gap between vertically stacked TiS_2 trilayers is one possible scenario leading to the surface TiS_2 to TiS transformation. The formation of H_2S molecules resulting from the interaction between the H-atoms from Ti-OH groups and S-H species has been predicted theoretically[46] but not observed experimentally. This strategy can also explain the role that defects play in determining the TiS_2 to TiS transformation temperature. S_v and Ti_i defects hinder the formation of the H_2S molecules because the energy of the intermediate state with Ti-OH at S_v-sites and Ti_i-OH at Ti_i-sites (cf. Figure 1) is even lower than that of the H_2O adsorbed state, as predicted theoretically.[46] That is, the system with Ti-OH at S_v-sites and Ti_i-OH groups is much stable, preventing the subsequent formation of H_2S. As a consequence, the annealing temperatures required for the TiS_2 to TiS transformation are higher than that found in 1*T*-TiS_2. As for the oxidation sample, the abundance of Ti-OH groups facilitates the formation of H_2S and thus the TiS_2 to TiS transformation. The TiS features are found on all four samples after 400 °C annealing, which means that the surface TiS_2 to TiS phase transition at higher annealing temperatures is defect insensitive because surface defects are most passivated at a temperature above 400 °C.

The surface-limited phase transformation may serve as an effective method toward the construction of high-quality heterostructures for device applications, overcoming the obstacles raised by the transfer process and the surface contamination.[47] In addition, this H_2O-assisted stripping process will enable the formation of a Janus TMDC monolayer with unique functionalities due to the breaking of the mirror asymmetry,[48] once chalcogen atoms can be restored. The adsorbed H_2O molecules on the surface of TMDCs as a result of air exposure may have a significant influence on their structural evolution, which could provide an alternative explanation for the modulation of chemical and physical properties in these materials. H_2S molecules, which are highly poisonous to the human body, may be released when MS_2 (M = transition metal) materials interact with water, such as electrochemical water splitting. Thus, special attention should be paid on the potential health risk against large amounts of exposure.

■ CONCLUSIONS

In summary, a thermally driven surface phase transformation from TiS_2 to TiS assisted by H_2O was observed by using a combination of PES, EPR spectroscopy, and Raman spectroscopy. The stripping of terminal S-atoms associated with the formation of H_2S molecules due to the chemical interaction between TiS_2 and surface-adsorbed H_2O molecules and the subsequent Ti_{uc} displacement are responsible for this transformation. The defects of S_v, Ti_i, and Ti-O species affect the phase transformation temperature by altering the TiS_2-H_2O chemical interaction at the surface of bulk TiS_2 crystals. S_v and Ti_i defects stabilize the Ti-OH at S_v-sties and Ti_i-OH group,

https://doi.org/10.1021/acs.jpcc.2c08140
J. Phys. Chem. C 2023, 127, 3462−3469

respectively, and prevent the formation of H_2S molecules, leading to higher phase transformation temperatures. In contrast, the abundance of Ti-OH species on $TiS_{2-x}O_x$ facilitates the phase transformation, leading to a room temperature phase transformation. Our findings not only provide a new perspective toward the construction of high-quality heterostructures by overcoming the obstacles raised by the transfer process and the surface contamination but also offer a H_2O-assisted etching strategy to synthesize the Janus TMDC materials.

■ ASSOCIATED CONTENT

Supporting Information

The Supporting Information is available free of charge at https://pubs.acs.org/doi/10.1021/acs.jpcc.2c08140.

XRD pattern, peak fitting parameters for Ti $2p_{3/2}$, S $2p_{3/2}$, and O 1s componentss of four studied samples extracted from the PES spectra and Raman spectra of the 500 °C annealed TiS_2 sample acquired from different spatial positions (PDF)

■ AUTHOR INFORMATION

Corresponding Authors

Yimin Xiong − *Department of Physics, School of Physics and Optoelectronics Engineering, Anhui University, Hefei, Anhui 230601, P. R. China; Hefei National Laboratory, Hefei, Anhui 230028, P. R. China*; Email: yxiong@ahu.edu.cn

Hai Xu − *Changchun Institute of Optics, Fine Mechanics and Physics, Chinese Academy of Sciences, Changchun, Jilin 130033, P. R. China; Center of Materials Science and Optoelectronics Engineering, University of Chinese Academy of Sciences, Beijing 100049, P. R. China;* orcid.org/0000-0002-4047-7087; Email: xuhai@ciomp.ac.cn

Liang Cao − *Anhui Province Key Laboratory of Condensed Matter Physics at Extreme Conditions, High Magnetic Field Laboratory, HFIPS, Chinese Academy of Sciences, Hefei, Anhui 230031, P. R. China;* orcid.org/0000-0001-7453-7060; Email: lcao@hmfl.ac.cn

Authors

Xue Chen − *Anhui Province Key Laboratory of Condensed Matter Physics at Extreme Conditions, High Magnetic Field Laboratory, HFIPS, Chinese Academy of Sciences, Hefei, Anhui 230031, P. R. China; University of Science and Technology of China, Hefei, Anhui 230026, P. R. China;* orcid.org/0000-0003-3469-3338

Meng Song − *Anhui Province Key Laboratory of Condensed Matter Physics at Extreme Conditions, High Magnetic Field Laboratory, HFIPS, Chinese Academy of Sciences, Hefei, Anhui 230031, P. R. China; University of Science and Technology of China, Hefei, Anhui 230026, P. R. China*

Liujiang Zhang − *Shanghai Synchrotron Radiation Facility (SSRF), Zhangjiang Laboratory, Shanghai Advanced Research Institute, Chinese Academy of Sciences, Shanghai 201204, P. R. China*

Ranran Zhang − *Anhui Province Key Laboratory of Condensed Matter Physics at Extreme Conditions, High Magnetic Field Laboratory, HFIPS, Chinese Academy of Sciences, Hefei, Anhui 230031, P. R. China*

Lei Zhang − *Anhui Province Key Laboratory of Condensed Matter Physics at Extreme Conditions, High Magnetic Field Laboratory, HFIPS, Chinese Academy of Sciences, Hefei, Anhui 230031, P. R. China*

Wei Tong − *Anhui Province Key Laboratory of Condensed Matter Physics at Extreme Conditions, High Magnetic Field Laboratory, HFIPS, Chinese Academy of Sciences, Hefei, Anhui 230031, P. R. China*

Yuyan Han − *Anhui Province Key Laboratory of Condensed Matter Physics at Extreme Conditions, High Magnetic Field Laboratory, HFIPS, Chinese Academy of Sciences, Hefei, Anhui 230031, P. R. China*

Xingyu Gao − *Shanghai Synchrotron Radiation Facility (SSRF), Zhangjiang Laboratory, Shanghai Advanced Research Institute, Chinese Academy of Sciences, Shanghai 201204, P. R. China*

Complete contact information is available at: https://pubs.acs.org/10.1021/acs.jpcc.2c08140

Author Contributions

○X.C. and M.S. contributed equally to this work.

Notes

The authors declare no competing financial interest.

■ ACKNOWLEDGMENTS

This work was supported by the National Key Research and Development Program of China (grant no. 2021YFA1600200), the National Natural Science Foundation of China (NSFC) (grant nos. 12074385, 12074372, and 12074386), Hefei Science Center, CAS (grant no. 2021HSC-KPRD003), Innovation Program for Quantum Science and Technology (grant no. 2021ZD0302802), and Anhui University start-up project (project no. S020318001/020). A portion of this work was supported by the High Magnetic Field Laboratory of Anhui Province and performed on the Steady High Magnetic Field Facilities, High Magnetic Field Laboratory, CAS.

■ REFERENCES

(1) Zeng, Q. S.; Liu, Z. Novel Optoelectronic Devices: Transition-Metal-Dichalcogenide-Based 2D Heterostructures. *Adv. Electron. Mater.* **2018**, *4*, No. 1700335.

(2) Su, J.; Li, G. D.; Li, X. H.; Chen, J. S. 2D/2D Heterojunctions for Catalysis. *Adv. Sci.* **2019**, *6*, No. 1801702.

(3) Das, P.; Fu, Q.; Bao, X. H.; Wu, Z. S. Recent advances in the preparation, characterization, and applications of two-dimensional heterostructures for energy storage and conversion. *J. Mater. Chem. A* **2018**, *6*, 21747−21784.

(4) Zhang, D. L.; Zeng, Z. X. S.; Tong, Q. J.; Jiang, Y.; Chen, S. L.; Zheng, B. Y.; Qu, J. Y.; Li, F.; Zheng, W. H.; Jiang, F.; et al. Near-Unity Polarization of Valley-Dependent Second-Harmonic Generation in Stacked TMDC Layers and Heterostructures at Room Temperature. *Adv. Mater.* **2020**, *32*, No. 1908061.

(5) Garcia, J. H.; Cummings, A. W.; Roche, S. Spin Hall Effect and Weak Antilocalization in Graphene/Transition Metal Dichalcogenide Heterostructures. *Nano Lett.* **2017**, *17*, 5078−5083.

(6) Ullah, F.; Sim, Y.; Le, C. T.; Seong, M. J.; Jang, J. I.; Rhim, S. H.; Khac, B. C. T.; Chung, K. H.; Park, K.; Lee, Y.; et al. Growth and Simultaneous Valleys Manipulation of Two-Dimensional $MoSe_2$-WSe_2 Lateral Heterostructure. *ACS Nano* **2017**, *11*, 8822−8829.

(7) Du, L. J.; Hasan, T.; Castellanos-Gomez, A.; Liu, G. B.; Yao, Y. G.; Lau, C. N.; Sun, Z. P. Engineering symmetry breaking in 2D layered materials. *Nat. Rev. Phys.* **2021**, *3*, 193−206.

(8) Voiry, D.; Goswami, A.; Kappera, R.; Silva, C. D. C. E.; Kaplan, D.; Fujita, T.; Chen, M. W.; Asefa, T.; Chhowalla, M. Covalent functionalization of monolayered transition metal dichalcogenides by phase engineering. *Nat. Chem.* **2015**, *7*, 45−49.

(9) Voiry, D.; Mohite, A.; Chhowalla, M. Phase engineering of transition metal dichalcogenides. *Chem. Soc. Rev.* **2015**, *44*, 2702−2712.
(10) Xiao, Y.; Zhou, M. Y.; Liu, J. L.; Xu, J.; Fu, L. Phase engineering of two-dimensional transition metal dichalcogenides. *Sci. China Mater.* **2019**, *62*, 759−775.
(11) Kappera, R.; Voiry, D.; Yalcin, S. E.; Branch, B.; Gupta, G.; Mohite, A. D.; Chhowalla, M. Phase-engineered low-resistance contacts for ultrathin MoS_2 transistors. *Nat. Mater.* **2014**, *13*, 1128−1134.
(12) Nourbakhsh, A.; Zubair, A.; Sajjad, R. N.; Tavakkoli, K. G. A.; Chen, W.; Fang, S.; Ling, X.; Kong, J.; Dresselhaus, M. S.; Kaxiras, E.; et al. MoS_2 Field-Effect Transistor with Sub-10 nm Channel Length. *Nano Lett.* **2016**, *16*, 7798−7806.
(13) Schulman, D. S.; Arnold, A. J.; Das, S. Contact engineering for 2D materials and devices. *Chem. Soc. Rev.* **2018**, *47*, 3037−3058.
(14) Chhowalla, M.; Jena, D.; Zhang, H. Two-dimensional semiconductors for transistors. *Nat. Rev. Mater.* **2016**, *1*, 16052.
(15) Zhu, H.; Wang, Q. X.; Zhang, C. X.; Addou, R.; Cho, K.; Wallace, R. M.; Kim, M. J. New Mo_6Te_6 Sub-Nanometer-Diameter Nanowire Phase from 2H-$MoTe_2$. *Adv. Mater.* **2017**, *29*, No. 1606264.
(16) Pawar, S. A.; Kim, D.; Lee, R.; Kang, S. W.; Patil, D. S.; Kim, T. W.; Shin, J. C. Efficient supercapacitor based on polymorphic structure of 1T'-Mo_6Te_6 nanoplates and few-atomic-layered 2H-$MoTe_2$: A layer by layer study on nickel foam. *Chem. Eng. J.* **2019**, *371*, 182−192.
(17) Cho, S.; Kim, S.; Kim, J. H.; Zhao, J.; Seok, J.; Keum, D. H.; Baik, J.; Choe, D. H.; Chang, K. J.; Suenaga, K.; et al. Phase patterning for ohmic homojunction contact in $MoTe_2$. *Science* **2015**, *349*, 625−628.
(18) Liu, Y. P.; Wang, H. T.; Cheng, L.; Han, N.; Zhao, F. P.; Li, P. R.; Jin, C. H.; Li, Y. G. TiS_2 nanoplates: A high-rate and stable electrode material for sodium ion batteries. *Nano Energy* **2016**, *20*, 168−175.
(19) Tao, H. W.; Zhou, M.; Wang, R. X.; Wang, K. L.; Cheng, S. J.; Jiang, K. TiS_2 as an Advanced Conversion Electrode for Sodium-Ion Batteries with Ultra-High Capacity and Long-Cycle Life. *Adv. Sci.* **2018**, *5*, No. 1801021.
(20) Wang, H.; Qiu, Z. Z.; Xia, W. Y.; Ming, C.; Han, Y. Y.; Cao, L.; Lu, J.; Zhang, P. H.; Zhang, S. B.; Xu, H.; et al. Semimetal or Semiconductor: The Nature of High Intrinsic Electrical Conductivity in TiS_2. *J. Phys. Chem. Lett.* **2019**, *10*, 6996−7001.
(21) Liu, T. T.; Zhang, X. K.; Xia, M. T.; Yu, H. X.; Peng, N.; Jiang, C.; Shui, M.; Xie, Y.; Yi, T. F.; Shu, J. Functional cation defects engineering in TiS_2 for high-stability anode. *Nano Energy* **2020**, *67*, No. 104295.
(22) Liu, T. T.; Peng, N.; Zhang, X. K.; Zheng, R. T.; Xia, M. T.; Yu, H. X.; Shui, M.; Xie, Y.; Shu, J. Controllable defect engineering enhanced bond strength for stable electrochemical energy storage. *Nano Energy* **2021**, *79*, No. 105460.
(23) Lu, J. H.; Lian, F.; Zhang, Y. X.; Chen, N.; Li, Y.; Ding, F.; Liu, X. J. Sulfide cluster vacancies inducing an electrochemical reversibility improvement of titanium disulfide electrode material. *J. Mater. Chem. A* **2020**, *8*, 6532−6538.
(24) Pawula, F.; Daou, R.; Hebert, S.; Lebedev, O.; Maignan, A.; Subedi, A.; Kakefuda, Y.; Kawamoto, N.; Baba, T.; Mori, T. Anisotropic thermal transport in magnetic intercalates FexTiS2. *Phys. Rev. B* **2019**, *99*, No. 085422.
(25) Chen, K.; Song, M.; Sun, Y. Y.; Xu, H.; Qi, D. C.; Su, Z. H.; Gao, X. Y.; Xu, Q.; Hu, J.; Zhu, J. F.; et al. Defects controlled doping and electrical transport in TiS_2 single crystals. *Appl. Phys. Lett.* **2020**, *116*, No. 121901.
(26) Siriwardane, R. V.; Poston, J. A. Interaction of H_2S with Zinc Titanate in the Presence of H_2 and Co. *Appl. Surf. Sci.* **1990**, *45*, 131−139.
(27) Endo, K.; Ihara, H.; Watanabe, K.; Gonda, S. I. XPS Study of One-Dimensional Compounds: TiS_3. *J. Solid State Chem.* **1982**, *44*, 268−272.
(28) Cao, L.; Wang, Y. Z.; Zhong, J. Q.; Han, Y. Y.; Zhang, W. H.; Yu, X. J.; Xu, F. Q.; Qi, D. C.; Wee, A. T. S. Electronic Structure, Chemical Interactions and Molecular Orientations of 3,4,9,10-Perylene-tetracarboxylic-dianhydride on TiO_2 (110). *J. Phys. Chem. C* **2011**, *115*, 24880−24887.
(29) Seah, M. P.; Gilmore, I. S.; Spencer, S. J. Quantitative XPS I. Analysis of X-ray photoelectron intensities from elemental data in a digital photoelectron database. *J. Electron Spectrosc. Relat. Phenom.* **2001**, *120*, 93−111.
(30) Oh, D. Y.; Choi, Y. E.; Kim, D. H.; Lee, Y. G.; Kim, B. S.; Park, J.; Sohn, H.; Jung, Y. S. All-solid-state lithium-ion batteries with TiS_2 nanosheets and sulphide solid electrolytes. *J. Mater. Chem. A* **2016**, *4*, 10329−10335.
(31) Okeil, S.; Yadav, S.; Bruns, M.; Zintler, A.; Molina-Luna, L.; Schneider, J. J. Photothermal catalytic properties of layered titanium chalcogenide nanomaterials. *Dalton Trans.* **2020**, *49*, 1032−1047.
(32) Simmons, G. W.; Beard, B. C. Characterization of Acid-Base Properties of the Hydrated Oxides on Iron and Titanium Metal-Surfaces. *J. Phys. Chem.* **1987**, *91*, 1143−1148.
(33) Hugenschmidt, M. B.; Gamble, L.; Campbell, C. T. The Interaction of H_2O with a TiO_2 (110) Surface. *Surf. Sci.* **1994**, *302*, 329−340.
(34) Erdem, B.; Hunsicker, R. A.; Simmons, G. W.; Sudol, E. D.; Dimonie, V. L.; El-Aasser, M. S. XPS and FTIR surface characterization of TiO_2 particles used in polymer encapsulation. *Langmuir* **2001**, *17*, 2664−2669.
(35) Stoch, J.; Gablankowskakukucz, J. The Effect of Carbonate Contaminations on the XPS O 1s Band-Structure in Metal Oxides. *Surf. Interface Anal.* **1991**, *17*, 165−167.
(36) Sodergren, S.; Siegbahn, H.; Rensmo, H.; Lindstrom, H.; Hagfeldt, A.; Lindquist, S. E. Lithium intercalation in nanoporous anatase TiO_2 studied with XPS. *J. Phys. Chem. B* **1997**, *101*, 3087−3090.
(37) Jaegermann, W.; Schmeisser, D. Reactivity of Layer Type Transition-Metal Chalcogenides Towards Oxidation. *Surf. Sci.* **1986**, *165*, 143−160.
(38) McCafferty, E.; Wightman, J. P. Determination of the concentration of surface hydroxyl groups on metal oxide films by a quantitative XPS method. *Surf. Interface Anal.* **1998**, *26*, 549−564.
(39) Ataca, C.; Ciraci, S. Dissociation of H_2O at the vacancies of single-layer MoS_2. *Phys. Rev. B* **2012**, *85*, No. 195410.
(40) Ghuman, K. K.; Yadav, S.; Singh, C. V. Adsorption and Dissociation of H_2O on Monolayered MoS_2 Edges: Energetics and Mechanism from ab Initio Simulations. *J. Phys. Chem. C* **2015**, *119*, 6518−6529.
(41) Tao, J. G.; Cuan, Q.; Gong, X. Q.; Batzill, M. Diffusion and Reaction of Hydrogen on Rutile TiO_2 (011)-2x1: The Role of Surface Structure. *J. Phys. Chem. C* **2012**, *116*, 20438−20446.
(42) Xu, C. B.; Yang, W. S.; Guo, Q.; Dai, D. X.; Chen, M. D.; Yang, X. M. Molecular Hydrogen Formation from Photocatalysis of Methanol on TiO_2 (110). *J. Am. Chem. Soc.* **2013**, *135*, 10206−10209.
(43) Zhu, H.; Wang, Q. X.; Cheng, L. X.; Addou, R.; Kim, J. Y.; Kim, M. J.; Wallace, R. M. Defects and Surface Structural Stability of $MoTe_2$ Under Vacuum Annealing. *ACS Nano* **2017**, *11*, 11005−11014.
(44) Keeble, D. J.; Thomsen, E. A.; Stavrinadis, A.; Samuel, I. D. W.; Smith, J. M.; Watt, A. A. R. Paramagnetic Point Defects and Charge Carriers in PbS and CdS Nanocrystal Polymer Composites. *J. Phys. Chem. C* **2009**, *113*, 17306−17312.
(45) Almeida, A. J.; Sahu, A.; Riedinger, A.; Norris, D. J.; Brandt, M. S.; Stutzmann, M.; Pereira, R. N. Charge Trapping Defects in CdSe Nanocrystal Quantum Dots. *J. Phys. Chem. C* **2016**, *120*, 13763−13770.
(46) Cucinotta, C. S.; Dolui, K.; Pettersson, H.; Ramasse, Q. M.; Long, E.; O'Brian, S. E.; Nicolosi, V.; Sanvito, S. Electronic Properties and Chemical Reactivity of TiS_2 Nanoflakes. *J. Phys. Chem. C* **2015**, *119*, 15707−15715.

https://doi.org/10.1021/acs.jpcc.2c08140
J. Phys. Chem. C 2023, 127, 3462−3469

(47) Novoselov, K. S.; Mishchenko, A.; Carvalho, A.; Neto, A. H. C. 2D materials and van der Waals heterostructures. *Science* **2016**, *353*, No. aac9439.
(48) Lu, A. Y.; Zhu, H. Y.; Xiao, J.; Chuu, C. P.; Han, Y. M.; Chiu, M. H.; Cheng, C. C.; Yang, C. W.; Wei, K. H.; Yang, Y. M.; et al. Janus monolayers of transition metal dichalcogenides. *Nat. Nanotechnol.* **2017**, *12*, 744−749.

https://doi.org/10.1021/acs.jpcc.2c08140
J. Phys. Chem. C 2023, 127, 3462−3469